

# Analytical Calculation of Eccentric Surface-Mounted Permanent-Magnet Motor Accounting for Iron Saturation

Zhaokai Li<sup>ID</sup>, Xiaoyan Huang<sup>ID</sup>, *Member, IEEE*, Ang Liu<sup>ID</sup>, Zhuo Chen<sup>ID</sup>, *Graduate Student Member, IEEE*, Yelong Yu<sup>ID</sup>, and Lijian Wu<sup>ID</sup>, *Senior Member, IEEE*

**Abstract**—This article presents an analytical model to predict the performance of eccentric surface-mounted permanent-magnet (ESPM) motor based on the nonlinear conformal mapping and reluctance network hybrid model (NCRHM). The proposed model can reveal the mutual influence of rotor eccentricity on the stator slotting and iron saturation accounting for the distortion of the equivalent current positions and air-gap path among the conformal mappings. The transformation between magnetic voltage drop of iron and equivalent current in the air region (including air-gap and slot region) is employed to consider the increased iron saturation due to the reduced air-gap length. Based on the proposed model, the electromagnetic performance including flux linkage, back electromotive force (EMF), torque, and unbalanced magnetic force (UMF) can be accurately predicted for any kind of rotor eccentricity. In addition, the NCRHM is compared with the complex permeance model (CPM) neglecting both iron saturation and the field distortion in conformal mappings, which exhibits the great advantage of NCRHM for ESPM motor. The excellent accuracy and great efficiency of the proposed model are validated by both finite-element analysis and test results.

**Index Terms**—Analytical model, conformal mapping, reluctance network, rotor eccentricity, saturation effect, slotting effect.

## I. INTRODUCTION

THE permanent-magnet (PM) motors have been widely used in the electric transportation, such as electric vehicles, electric aircraft, and high-speed train due to the advantage of high power density and efficiency. However, the excellent performance of the PM motor is often deteriorated due to the rotor eccentricity, which comes from the manufacture imprecision, structure deformation, bearing tolerances, etc. Hence, it is significant for manufacturers and researchers to account for the influence of rotor eccentricity when designing the PM motor or in the fault diagnosis [1].

Manuscript received 3 January 2022; revised 28 February 2022; accepted 26 March 2022. Date of publication 1 April 2022; date of current version 2 August 2022. This work was supported in part by the National Natural Science Foundation of China under Grant 51922095, in part by Zhejiang Provincial Ten-Thousand-Talent Plan under Grant 2019R52003, and in part by the Zhejiang Provincial Natural Science Foundation of China under Grant LQ22E070003. (Corresponding author: Xiaoyan Huang.)

The authors are with the Zhejiang Provincial Key Laboratory of Electrical Machine Systems, College of Electrical Engineering, Zhejiang University, Hangzhou 310027, China (e-mail: lzk\_zju@zju.edu.cn; xiaoyanhuang@zju.edu.cn; a\_liu@zju.edu.cn; z.chen@zju.edu.cn; yuyelong@zju.edu.cn; ljw@zju.edu.cn).

Digital Object Identifier 10.1109/TTE.2022.3164078

2332-7782 © 2022 IEEE. Personal use is permitted, but republication/redistribution requires IEEE permission. See <https://www.ieee.org/publications/rights/index.html> for more information.

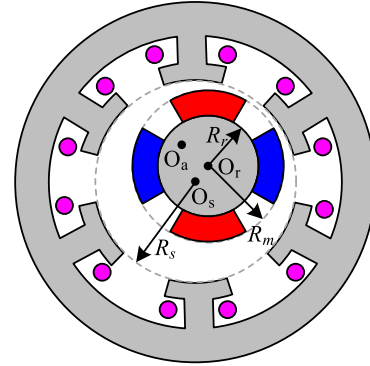


Fig. 1. Schematic view of ESPM motor with rotor eccentricity in the S-plane.

In general, the rotor eccentricity can be classified as static eccentricity, dynamic eccentricity, and mix eccentricity. They are defined according to the position of the rotating axis. Fig. 1 shows the schematic view of the eccentric surface-mounted permanent-magnet (ESPM) motor, where the rotor center  $O_r$  is displaced from the stator center  $O_s$ . It illustrates the differences among the three rotor eccentricities. For the static eccentricity, the rotating axis of rotor  $O_a$  is placed at the rotor center  $O_r$ . For the dynamic eccentricity,  $O_a$  coincides with the stator center  $O_s$ . As for the mix eccentricity, it is the most general situation when  $O_a$  is placed at any position in the motor except  $O_r$  and  $O_s$  [2].

In order to predict the performance of the eccentric motor, different models have been introduced to account for the rotor eccentricity. The finite-element method (FEM) can precisely describe the change of magnetic field in the PM motor when rotor eccentricity occurs, but it is time-consuming [3]. Based on the FEM, the impulse method is developed to show the frequency response under rotor eccentricity [4]. For modeling the axial flux PM machine with eccentricity, field reconstruction method was proposed to calculate the air-gap field distribution, which can achieve the same accuracy as FEM with lower computational burden [5].

Winding function method directly calculates the air-gap flux density using the geometry of eccentric air-gap, and it has been investigated in the induction motors [6] and synchronous reluctance motors [7]; however, this method is not suitable for

ESPM motor due to the relative large air-gap. The perturbation theory combined with analytical models is used to analyze the slotless ESPM motors [8]. The slotting effect was considered using the boundary perturbation method [9], relative permeance model [10], or subdomain model [11]. However, these models neglect iron saturation. Since the local iron saturation in the eccentric motor is significant due to the reduced air-gap length, it is necessary to consider the saturation effect in the analysis of eccentric motor. Dorrell [12] found that unbalanced magnetic force (UMF) in the induction motor can be attenuated due to tooth-tip saturation. In [13], the air-gap flux density is decreased when considering iron saturation in the ESPM motor. The magnetic circuit model can account for the saturation effect for electric motors, but there are few research articles for the eccentric motors. The main difficulty and limitation for the magnetic circuit model are the variation of air-gap reluctance and dynamic network at different rotor positions, leading to the low accuracy for calculating the air-gap field.

Conformal mapping is a powerful tool to transform the eccentric air-gap into concentric air-gap. Jalali *et al.* [2] introduced the bilinear conformal mapping to obtain the eccentric magnetic field for slotless ESPM motor. Li *et al.* [10] developed the relative permeance function based on conformal mapping to show the influence of eccentricity on the radial flux density. Alam and Abbaszadeh [14] modified the complex permeance model (CPM) to account for the rotor eccentricity, but it neglects the influence of rotor eccentricity on the slotting effect. In addition, it can introduce errors when introducing the saturation factor to represent the iron saturation. In addition, the modification of air-gap length and tooth tips was another choice to represent iron saturation and the CPM was used to account for stator slotting and rotor eccentricity [13]. Similarly, Mahmoud and Bianchi [15] extended the combination of CPM and saturation factor to synchronous reluctance motors.

There is strong coupling among rotor eccentricity, slotting effect, and saturation effect in the ESPM motor. To investigate their mutual relationship on the motor performance, the nonlinear conformal mapping and reluctance network hybrid model (NCRHM) is developed in this article to account for these remarkable features. First, there are four conformal mappings to transform the slotted eccentric air-gap domain in the ESPM motor into the slotless annulus, where the Hague's equation is applied to obtain the analytical field solution. It can precisely exhibit the change of slotting effect due to rotor eccentricity and give the physical insight for eccentricity effect. The reluctance network is introduced to represent the magnetic voltage drop. It decreases the value of air-gap field generated from the equivalent current of saturation. The proposed model is used to analyze a 10-pole/12-slot ESPM motor with static, dynamic, and mix eccentricity, whose accuracy and efficiency are validated by the FEM. Then, a prototype is built to verify the effectiveness of NCRHM.

## II. NONLINEAR HYBRID MODEL

The NCRHM has the following assumptions: 1) the relative permeability of PM is 1 with linear property and 2) the end

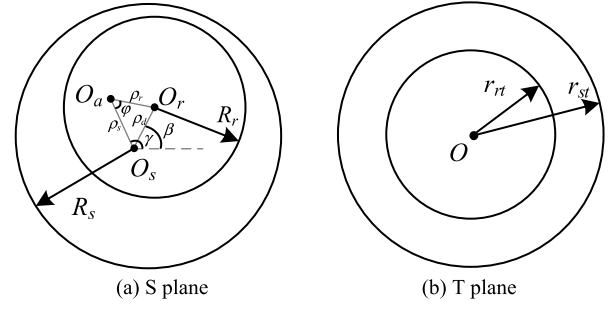


Fig. 2. General symbols of bilinear mapping for the slotless SPM motor: (a) eccentric air-gap and (b) concentric air-gap.

effect is neglected. Four conformal mappings are introduced to convert the air-gap domain of the ESPM motor in the S-plane to that in the  $\Psi$ -plane and obtain the air-gap field distribution. Even under no-load condition, the saturation level in the stator is significantly increased due to rotor eccentricity, which is represented by the equivalent current of saturation.

### A. Bilinear Mapping

Bilinear mapping is widely-used to transform two eccentric circles to two concentric circles [14]. The general form of bilinear mapping is shown as

$$T = \frac{aS + b}{S + d} \quad (1)$$

where

$$a = \frac{(R_s^2 - c_0^2)(\rho_d + c_0)}{R_s[(\rho_d + c_0)^2 - R_r^2]} e^{-j\beta} \quad (2)$$

$$b = \frac{(c_0^2 - R_s^2)[(\rho_d + c_0)\rho_d - R_r^2]}{R_s[(\rho_d + c_0)^2 - R_r^2]} \quad (3)$$

$$d = c_0 e^{j\beta} \quad (4)$$

$$e_0 = \frac{\rho_d^2 + R_s^2 - R_r^2}{2\rho_d} \quad (5)$$

$$c_0 = -e_0 - \sqrt{e_0^2 - R_s^2}.$$

Fig. 2 illustrates the symbols of the ESPM motor using bilinear mapping when neglecting the stator slots and PMs. The stator bore and rotor outer surface are the two circles to determine the parameters of bilinear mapping, whose radii are  $R_s$  and  $R_r$ , respectively. In Fig. 2,  $\rho_s$ ,  $\rho_r$ , and  $\rho_d$  are the distances of  $O_s O_a$ ,  $O_a O_r$ , and  $O_s O_r$ , respectively.  $\gamma$  is the angle between  $O_s O_a$  and horizon axis.  $\beta$  is the angle between  $O_s O_r$  and horizon axis.  $\phi$  is the angle between  $O_a O_r$  and  $O_a O_s$ , where  $\phi(t) = \omega t + \phi_0$ .  $\omega$  is the angular speed of the rotor and  $\phi_0$  is the initial rotor position. The rotor eccentricity ratio is defined as

$$\varepsilon = \frac{\rho_s}{\rho_s + \rho_r}. \quad (6)$$

It is noted that the static eccentricity and dynamic eccentricity are represented by  $\varepsilon = 1$  and  $\varepsilon = 0$ , respectively. For the mix eccentricity,  $0 < \varepsilon < 1$ .

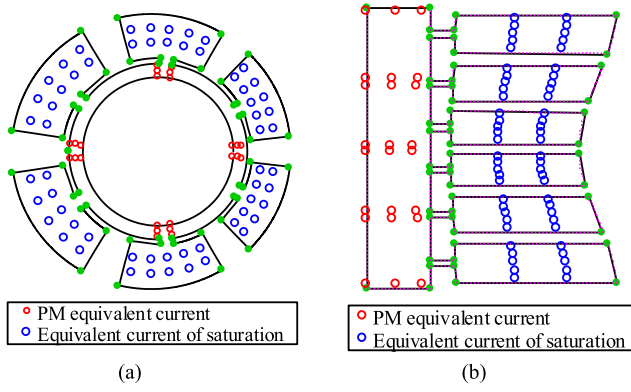


Fig. 3. Air-gap region and slot region of ESPM motor using the logarithmic complex function: (a) T-plane and (b) Z-plane.

For the slotted ESPM motor, the same bilinear mapping is used to obtain a concentric air-gap using (1)–(5). Fig. 3(a) shows the concentric air-gap in the T-plane, which is transformed from the eccentric motor in the S-plane of Fig. 1. It is noted that the slot size and slot opening in the T-plane are changed after the bilinear mapping. It means that the slotting effect is influenced by rotor eccentricity, which is neglected in the CPM. Such differences can be more clearly observed in Fig. 3(b), where the concentric air-gap is transformed into a multilateral polygon using the logarithmic complex function

$$Z = \log(T). \quad (7)$$

### B. SC Mapping

Schwarz-Christoffel (SC) mapping shows great accuracy in transforming the rectangular area in the W-plane to the interior of multilateral polygon in the Z-plane. The general form of SC mapping is defined as

$$Z = Z_0 + Z_1 \int_{w_0}^w \prod_{k=1}^{n-1} (W - w_k)^{\alpha_j - 1} dW \quad (8)$$

where  $Z_0$ ,  $Z_1$ ,  $w_1$ , ...,  $w_{n-1}$ ,  $\alpha_1$ , ...,  $\alpha_{n-1}$  are the SC parameters [16]. These parameters can be calculated using SC toolbox in the MATLAB. Fig. 4(a) shows the rectangular domain representing air-gap and slot in the W-plane, which is transformed from the multilateral polygon in the Z-plane of Fig. 3(b). It is noted that the position of the equivalent currents in the W-plane is nonuniformly distributed in different slots. After the inverse SC mapping, the exponential complex function is used to map the rectangle in the W-plane to the annular domain in the  $\psi$ -plane [see Fig. 4(b)]

$$\psi = e^{-j \left[ \frac{2}{\Delta x} \left( W - j \frac{\Delta y}{2} \right) - 1 \right] \pi} \quad (9)$$

where  $\Delta x$  and  $\Delta y$  represent the length and width of the rectangle in the W domain.

### C. Analytical Solution of Air-Gap Field

The four conformal mappings have connected the original eccentric motor in the S-plane with the concentric annulus in the  $\psi$ -plane. As the equivalent current of PM, coil, and

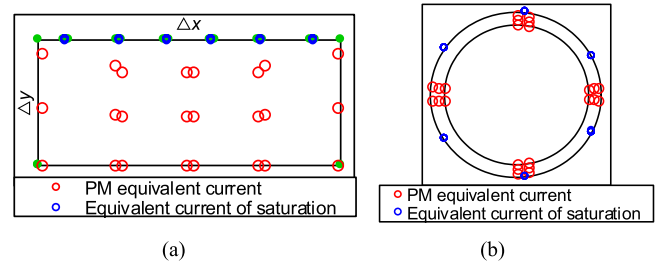


Fig. 4. Air-gap region and slot region of ESPM motor using the exponential complex function: (a) W-plane and (b)  $\psi$ -plane.

saturation in the original S-plane are mapped into  $\psi$ -plane, the Hague's equation is used to analytically obtain the air-gap field in the slotless annulus of  $\psi$ -plane. Using the inverse conformal mapping from  $\psi$ -plane to S-plane, the magnetic field in the concentric motor can be accordingly obtained.

According to the superposition principle, the total air-gap field in the ESPM motor can be regarded as the sum of the magnetic field generated from those equivalent currents of PM, coil, and saturation. The PMs with radial magnetization are equivalently replaced by the equivalent currents along the lateral side of the magnet. The value of PM equivalent current can be calculated as

$$i_{PM} = \frac{B_r h_m}{\mu_r n_{PM}} \quad (10)$$

where  $\mu_r$ ,  $h_m$ , and  $B_r$  are the permeability, thickness, and remanence of the PM.  $n_{PM}$  is the number of PM equivalent current.

For the equivalent current of coil, it is replaced by one or two dot current at the center of each slot depending on winding layout, and the value of coil equivalent current is obtained from the input current. The equivalent current of saturation will be introduced in Section II-D.

Then, the magnetic vector potential  $A_z(r_{p\psi}, \alpha_{p\psi})$  produced by the single equivalent current  $i_c(r_{c\psi}, \alpha_{c\psi})$  representing PM, coil, or iron saturation in the concentric slotless air-gap of  $\psi$ -plane is manipulated as

$$A_z(r_{p\psi}, \alpha_{p\psi}) = \frac{-\mu_0 i_c(r_{c\psi}, \alpha_{c\psi})}{2\pi} \times \left\{ \frac{1}{k} \cos[k(\alpha_{p\psi} - \alpha_{c\psi})] + \sum_{k=1}^{+\infty} \left( \frac{r_{c\psi}^{2k} + r_r^{2k}}{r_s^{2k} - r_r^{2k}} \frac{r_{p\psi}^k}{r_{c\psi}^k} + \frac{r_{c\psi}^{2k} + r_s^{2k}}{r_s^{2k} - r_r^{2k}} \frac{r_r^{2k}}{r_{p\psi}^k r_{c\psi}^k} \right) - \ln(d_{pc}) \right\} \quad (11)$$

where  $\mu_0$  is the vacuum permeability.  $r_s$  and  $r_r$  represent the inside and outside radii of annulus.  $d_{pc}$  is the distance between the dot current position and the position for calculating the air-gap field [19]. Since the conformal mapping preserves the magnetic potential value, the magnetic vector potential  $A_z(r_{ps}, \alpha_{ps})$  in the S-plane is calculated as

$$A_z(r_{ps}, \alpha_{ps}) = A_z(r_{p\psi}, \alpha_{p\psi}). \quad (12)$$

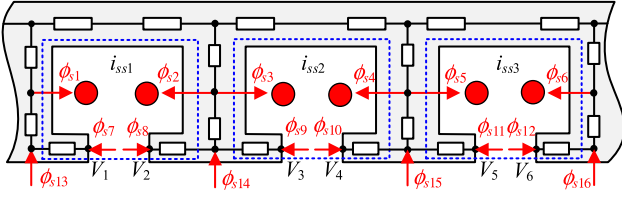


Fig. 5. Transformation between the magnetic voltage drop and equivalent current of saturation.

The radial and tangential components of air-gap field in the  $\psi$ -plane are also obtained from  $A_z(r_{p\psi}, \alpha_{p\psi})$

$$\begin{aligned} B_{p\psi r}(r_{p\psi}, \alpha_{p\psi}) &= \frac{\partial A_z(r_{p\psi}, \alpha_{p\psi})}{r \partial \alpha} \\ B_{p\psi \alpha}(r_{p\psi}, \alpha_{p\psi}) &= -\frac{\partial A_z(r_{p\psi}, \alpha_{p\psi})}{\partial r}. \end{aligned} \quad (13)$$

The solution of (13) presents the magnetic field in the polar coordinates, and it is transformed to the Cartesian coordinates

$$\begin{aligned} B_{p\psi x}(x_{p\psi}, y_{p\psi}) &= B_{p\psi r} \cos(\alpha_{p\psi}) - B_{p\psi \alpha} \sin(\alpha_{p\psi}) \\ B_{p\psi y}(x_{p\psi}, y_{p\psi}) &= B_{p\psi r} \sin(\alpha_{p\psi}) + B_{p\psi \alpha} \cos(\alpha_{p\psi}). \end{aligned} \quad (14)$$

Then, the complex permeance function  $\lambda$  is introduced to connect the flux density in  $\psi$ -plane and S-plane. The magnetic field  $B_{psx}$  and  $B_{psy}$  in the S-plane can be inversely mapped from  $B_{p\psi x}$  and  $B_{p\psi y}$  in the  $\psi$ -plane

$$\begin{aligned} B_{psx}(x_{ps}, y_{ps}) &= \lambda_r B_{p\psi x} - \lambda_i B_{p\psi y} \\ B_{psy}(x_{ps}, y_{ps}) &= \lambda_i B_{p\psi x} + \lambda_r B_{p\psi y} \end{aligned} \quad (15)$$

where

$$\lambda = \frac{1}{\frac{\partial w}{\partial \psi}} \frac{1}{\frac{\partial z}{\partial w}} \frac{\partial z}{\partial t} \frac{\partial t}{\partial s} = \lambda_r + i \lambda_i \quad (16)$$

$$\frac{\partial w}{\partial \psi} = \frac{2\pi}{j \Delta x} r_{\psi} e^{j\alpha_{\psi}} \quad (17)$$

$$\frac{\partial z}{\partial w} = \text{evaldiff}(f, w) \quad (18)$$

$$\frac{\partial z}{\partial t} = \text{re}^{j\theta} \quad (19)$$

$$\frac{\partial t}{\partial s} = \frac{R_s^2 - c_0^2}{R_s(s + c_0 e^{j\varphi})^2}. \quad (20)$$

The complex permeance function  $\lambda$  is the connection between the slotted and slotless air-gap fields. The influence of motor geometry on  $\lambda$  can be directly obtained using (16)–(20) while the slotless air-gap field has simple expression in [17]. According to the waveform of complex permeance function, it is easy and clear to analyze the variation of slotted air-gap field from the simple slotless air-gap field and investigate the performance of ESPM motor. Accordingly, the radial and tangential flux densities in the  $\psi$ -plane are obtained as

$$\begin{aligned} B_{psr}(r_{p\psi}, \alpha_{p\psi}) &= B_{psx} \cos(\alpha_{p\psi}) + B_{psy} \sin(\alpha_{p\psi}) \\ B_{ps\alpha}(r_{p\psi}, \alpha_{p\psi}) &= -B_{psx} \sin(\alpha_{p\psi}) + B_{psy} \cos(\alpha_{p\psi}). \end{aligned} \quad (21)$$

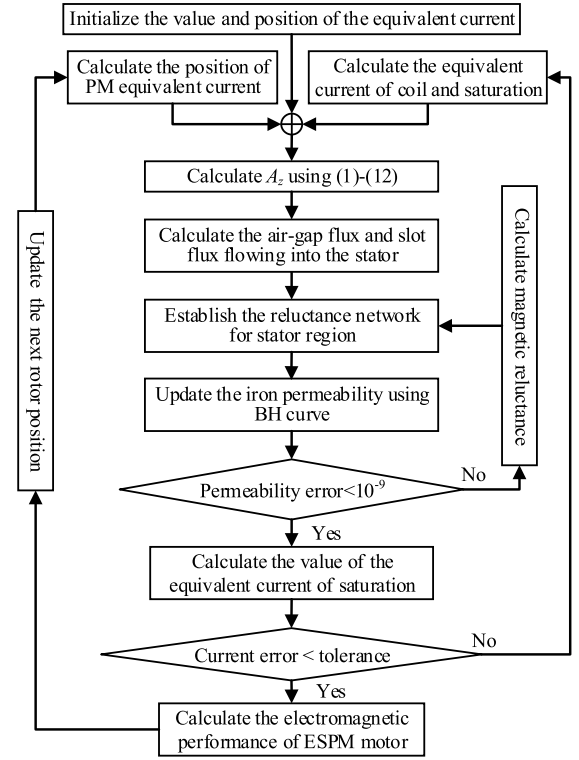


Fig. 6. Flowchart of calculating the equivalent current of saturation.

#### D. Iron Saturation

In order to consider the saturation effect, the equivalent current of saturation  $i_{ss}$  is introduced to replace the magnetic voltage drop, as shown in Fig. 5. It is located at the same position as the equivalent current of coil and is calculated using

$$i_{ssk} = V_{s(2k)} - V_{s(2k-1)} \quad (22)$$

where  $V_{s(2k)}$  and  $V_{s(2k-1)}$  are the magnetic potential in the tooth tip.

In order to obtain the magnetic voltage drop in the stator region, the reluctance network is used to show the flux path in the stator yoke, tooth body, and tooth tip (see Fig. 5). The air-gap flux and slot flux are obtained using the magnetic vector potential  $A_z(r_{ps}, \alpha_{ps})$  in the S-plane

$$\varphi_{sj} = [A_z(r_{ps1}, \alpha_{ps1}) - A_z(r_{ps2}, \alpha_{ps2})] l_{ef} \quad (23)$$

where  $(r_{ps1}, \alpha_{ps1})$  and  $(r_{ps2}, \alpha_{ps2})$  represent the specified area for calculating flux.

#### E. Calculation Process

The general solution of NCRHM is derived from the calculation of reluctance network in Fig. 5 using

$$f(\mathbf{V}) = \mathbf{A} \mathbf{\Lambda} \mathbf{A}^T \mathbf{V} - \Phi_s = \mathbf{0} \quad (24)$$

where  $\mathbf{V}$ ,  $\mathbf{A}$ ,  $\mathbf{\Lambda}$ , and  $\Phi_s$  are the matrices of node magnetic potential, incidence, branch permeance, and the air-gap flux  $\varphi_{sj}$ , respectively. Fig. 6 gives the general solving process. The initial value of equivalent current of saturation is zero, and



therefore, the linear analytical solution of air-gap field can be obtained in the first step. Then, an inner solving loop is required to obtain the magnetic voltage drop of stator based on  $B-H$  curve of iron. Accordingly, the equivalent current of saturation is updated from the magnetic voltage drop in the external loop. If the equivalent current is not convergent, the air-gap flux and slot flux should be calculated again in the inner loop using the reluctance network in Fig. 5. The Newton–Raphson method is often employed to accelerate the convergence speed, and therefore, the air-gap field of ESPM motor is obtained using (11)–(21). It is noted that the tolerance of current error in Fig. 6 depends on the required accuracy for predicting the air-gap field. For most ESPM motors, the criterion of “Error of current  $< 0.1\%$ ” is used to obtain a satisfactory result based on practice.

### III. ELECTROMAGNETIC PERFORMANCE CALCULATION

The flux linkage can be calculated from the integral of the air-gap field along the coil pitch belonging to the same phase

$$\psi_p = N_c R_s l_{ef} \int_{\alpha_i}^{\alpha_i + \tau} B_{sr}(R_s, \alpha) d\alpha \quad (25)$$

where  $l_{ef}$  is the effective length of stator in the axial direction.  $\tau$  is the coil pitch, and  $\alpha_i$  is the initial tangential position of the coil.

Hence, according to Faraday’s law, the back electromotive force (EMF) of the ESPM motor can be calculated using the derivative of the flux linkage

$$E_p = -\frac{d\psi_p}{dt}. \quad (26)$$

The torque of the motor can be obtained based on the Maxwell tensor theory, which is equal to the integral of product between radial and tangential flux densities along the air-gap circle

$$T = \frac{1}{\mu_0} l_{ef} r^2 \int_0^{2\pi} B_{sr}(r, \alpha) B_{st}(r, \alpha) d\alpha. \quad (27)$$

The rotor eccentricity will significantly influence the UMF. Hence, it is necessary to evaluate the change of UMF due to eccentricity [18]. The force in the  $x$ - and  $y$ -direction can be calculated using the Maxwell tensor

$$F_x = \frac{rl_{ef}}{2\mu_0} \int_0^{2\pi} [(B_{st}^2 - B_{sr}^2) \cos(\alpha) + 2B_{sr}B_{sa} \sin(\alpha)] d\alpha \quad (28)$$

$$F_y = \frac{rl_{ef}}{2\mu_0} \int_0^{2\pi} [(B_{st}^2 - B_{sr}^2) \sin(\alpha) - 2B_{sr}B_{sa} \cos(\alpha)] d\alpha. \quad (29)$$

The modulus of the UMF can be, therefore, determined by

$$F = \sqrt{F_x^2 + F_y^2}. \quad (30)$$

### IV. FINITE-ELEMENT AND EXPERIMENTAL VALIDATION

A 10-pole/12-slot ESPM motor is designed and analyzed to validate the proposed model. The motor parameters are given in Table I. The FEM calculation is carried out in JMAG [see Fig. 7(a)]. Then, a prototype with static eccentricity is built and tested in Fig. 7(b) and (c).

TABLE I  
MAIN PARAMETERS OF ESPM MOTOR

Parameter	Value	Unit
Stator outer radius	60	mm
Stator inner radius	32	mm
Airgap length	1	mm
Slot opening	2	mm
Stator yoke height	6	mm
Tooth body width	7.95	mm
Magnet thickness	3	mm
Number of pole pairs	5	
Number of slots	12	
Active length	70	mm
Rated speed	3000	rpm

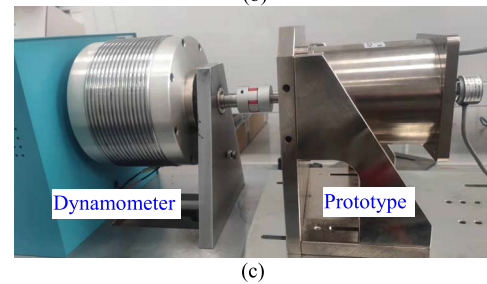
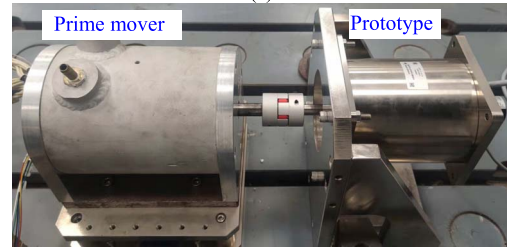
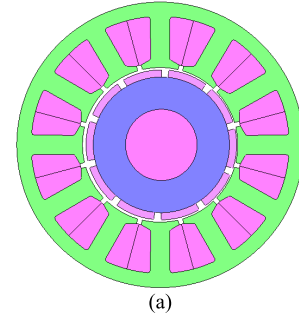


Fig. 7. ESPM motor in the simulation and in the test: (a) JMAG simulation; (b) back EMF test; and (c) torque test.

First, the conformal mappings for NCRHM and CPM are compared to show the errors of neglecting the field distortion in conformal mappings according to (15). The distance between center and rotor center is 0.5 mm. In Fig. 8(a), the position from S-plane to  $\Psi$ -plane using NCRHM is different from that using CPM while their complex permeance functions are the same in Fig. 8(b) and (c). Such difference leads to less accurate calculation of flux density using CPM, as shown in Fig. 9. Both radial and tangential flux densities predicted using NCRHM match well with FEM results due to considering iron saturation and applying the more accurate conformal mapping. CPM prediction has significant difference in the nearest region

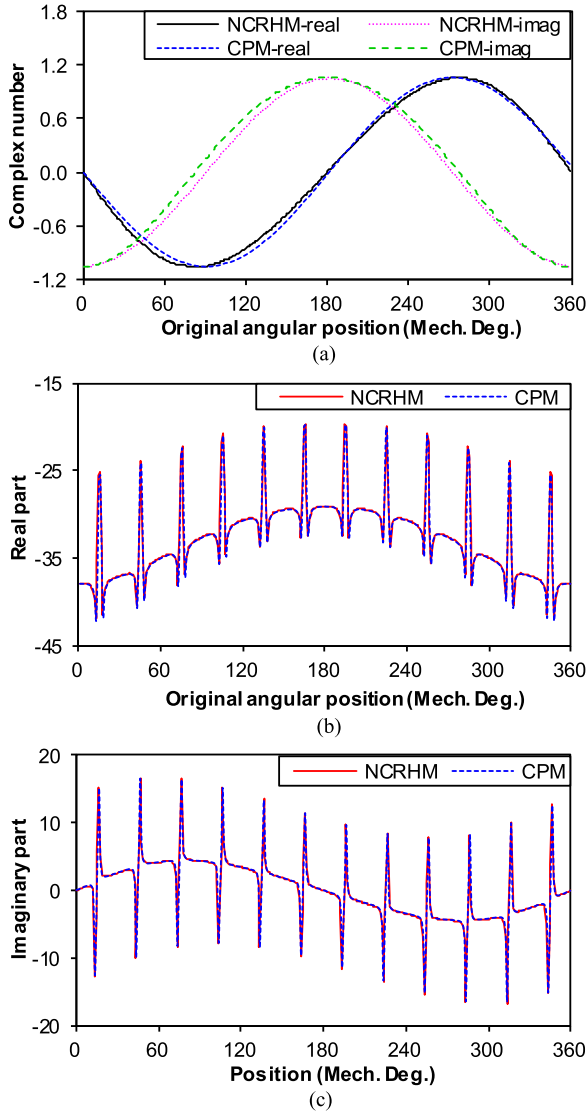


Fig. 8. Comparison of NCRHM and CPM during conformal mapping: (a) position; (b) real part of complex permeance function  $\lambda$ ; and (c) imaginary part of complex permeance function  $\lambda$ .

of the eccentric air-gap. In Fig. 8(b) and (c), 12 steep peaks representing slotting effect are lying on the gentle slope representing rotor eccentricity. According to the proposed model, the rotor center should get close to the stator bore at the angular position of  $0^\circ$ , and therefore, the corresponding air-gap field in the radial direction will become larger, as shown in Fig. 9(a).

Then, the variation of harmonic flux density to the eccentric distance of rotor center and stator center is investigated and analyzed using Fig. 10. The eccentric distance has negligible influence on the major harmonic of radial flux density, but the increased eccentric distance can reduce the major harmonic of tangential flux density in Fig. 10. However, in Fig. 11, the 6th and 16th harmonic of radial flux density will increase as the eccentric distance grows. Figs. 10 and 11 illustrate that it is important to select the useful and sensitive harmonic flux density for the fault severity assessment of rotor eccentricity [20].

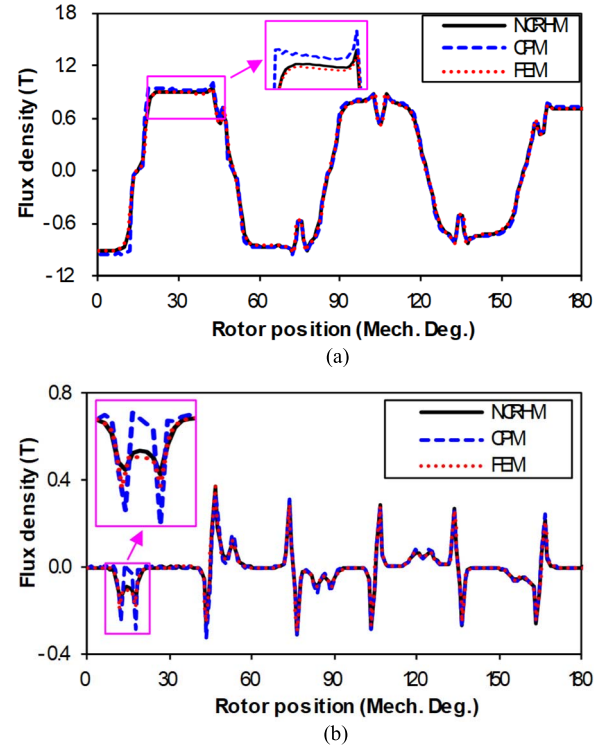


Fig. 9. Flux density predicted using NCRHM, CPM, and FEM along the center line of the air-gap under open-circuit condition: (a) radial flux density and (b) tangential flux density.

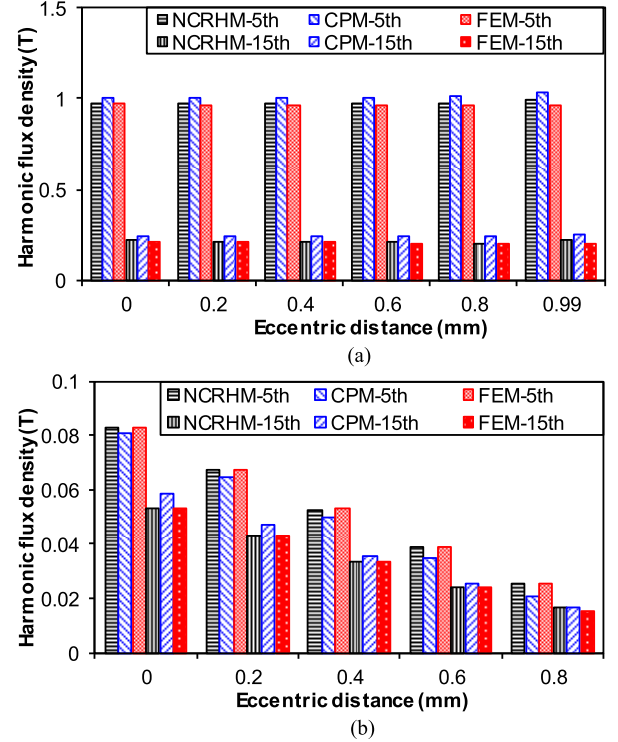


Fig. 10. Variation of major harmonic flux density to the eccentric distance of rotor center and stator center: (a) radial direction and (b) tangential direction.

Figs. 12 and 13 give the comparison of phase flux linkage and phase back EMF under static eccentricity ( $\varepsilon = 1$ ) using NCRHM and CPM. CPM has larger errors than NCRHM for

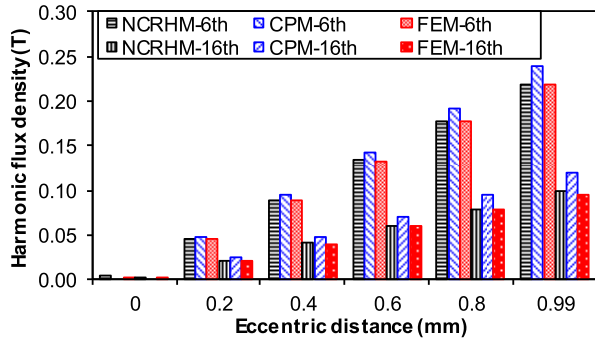


Fig. 11. Variation of 6th and 16th harmonic of radial flux density to the eccentric distance of rotor center and stator center.

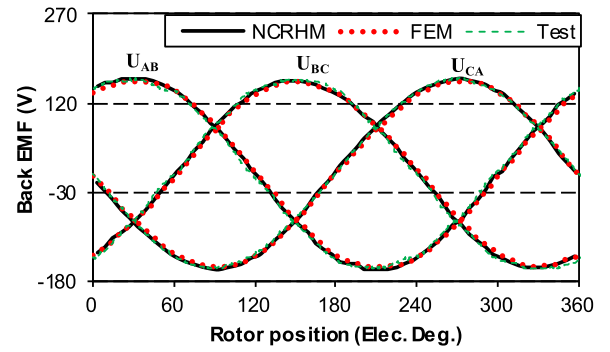


Fig. 14. Measured line back EMF under static eccentricity.

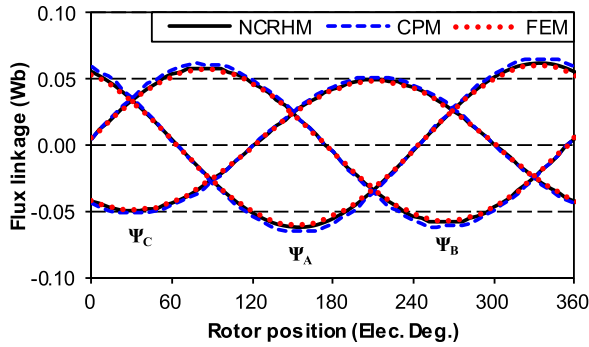


Fig. 12. Comparison of phase flux linkage using NCRHM and CPM under static eccentricity.

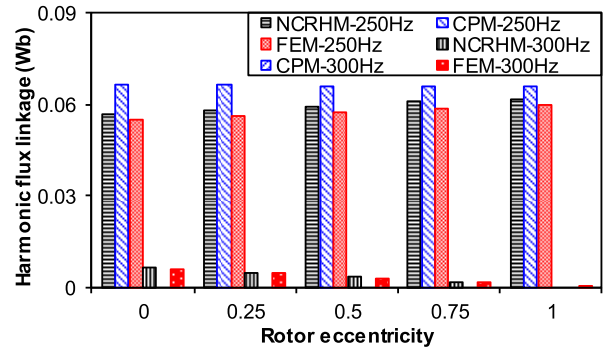


Fig. 15. Variation of harmonic flux linkage to rotor eccentricity ratio.

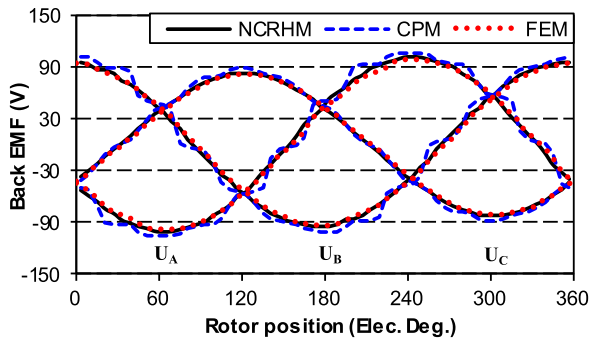


Fig. 13. Comparison of phase back EMF using NCRHM and CPM under static eccentricity.

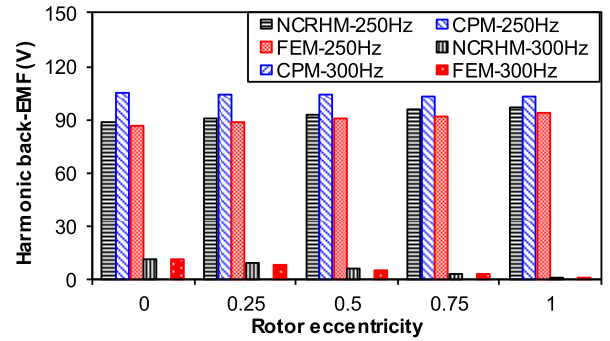


Fig. 16. Variation of harmonic back EMF to rotor eccentricity ratio.

both flux linkage and back EMF. The amplitude of flux linkage and back EMF in phase C are much smaller than those in phase A and phase B. However, the line back EMF in phases A, B, and C has similar amplitude, as shown in Fig. 14. Meanwhile, the NCRHM prediction of line back EMF agrees well with the experimental result. Figs. 15 and 16 illustrate the major harmonic components of flux linkage and back EMF for static ( $\varepsilon = 1$ ), dynamic ( $\varepsilon = 0$ ), and mix eccentricity ( $\varepsilon = 0.25, 0.5, 0.75$ ). It can be seen that NCRHM predictions for the fundamental flux linkage and back EMF agree well with FEM results while CPM predictions show much higher amplitude than FEM results under any rotor eccentricity.

Figs. 17–19 show the cogging torque waveform at different rotor eccentricity. NCRHM achieves high accuracy for predicting cogging torque even the value of cogging torque is small in 10-pole/12-slot motor, but the errors of CPM can reach over 80%. When the ESPM motor with static eccentricity is operated at constant load torque using maximum torque per ampere (MTPA) control, the amplitudes of three-phase current are not the same [22]. As the predicted back EMF of phase C is the smallest in Fig. 12, the measured current amplitude of phase C is the largest to produce the constant torque from the experiment (see Fig. 20). Then, the variation of average torque to current is obtained from both simulation and experiment in Fig. 21. It can be seen that NCRHM agrees well with both FEM and experimental result.

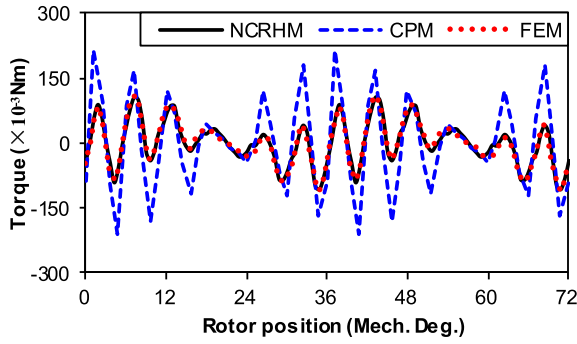


Fig. 17. Cogging torque predicted using NCRHM, CPM, and FEM at static eccentricity ( $\varepsilon = 1$ ).

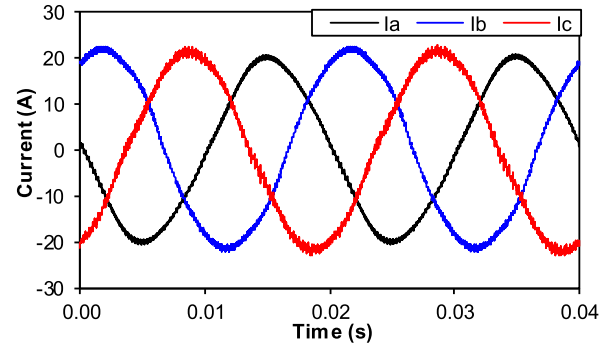


Fig. 20. Measured current waveform of ESPM motor at static eccentricity for on-load condition.

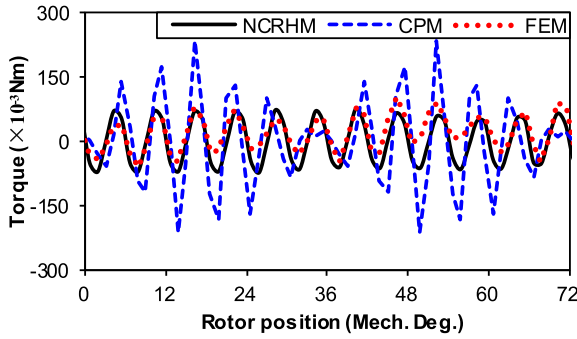


Fig. 18. Cogging torque predicted using NCRHM, CPM, and FEM under mix eccentricity ( $\varepsilon = 0.5$ ).

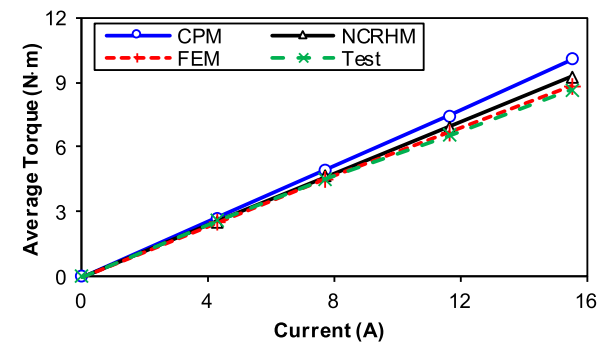


Fig. 21. Variation of average torque to current at static eccentricity.

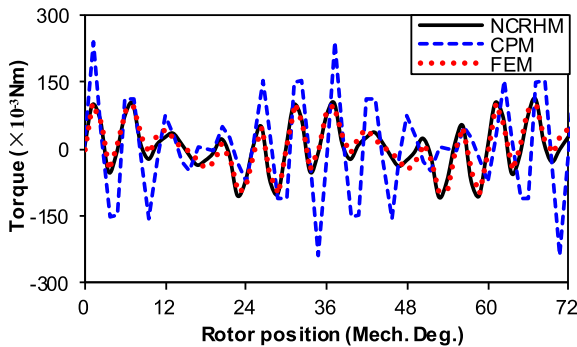


Fig. 19. Cogging torque predicted using NCRHM, CPM, and FEM at dynamic eccentricity ( $\varepsilon = 0$ ).

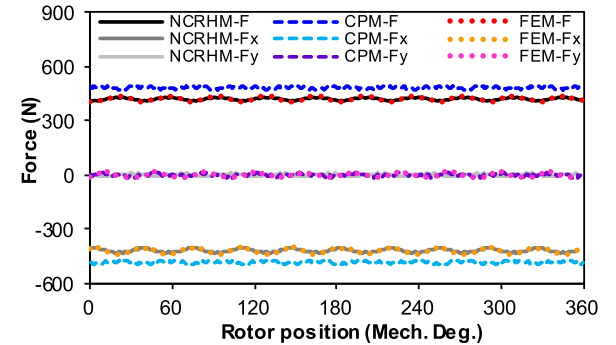


Fig. 22. UMF predicted using NCRHM, CPM, and FEM under static eccentricity for open-circuit condition.

The waveform of unbalance magnetic force and major harmonic components predicted using NCRHM, CPM, and FEM under different kinds of rotor eccentricity are compared in Figs. 22 and 23 for open-circuit condition. CPM predicts slightly higher value of UMF while NCRHM predictions agree well with FEM results. The rotor eccentricity can significantly affect the UMF. When the rotor eccentricity ratio  $\varepsilon$  becomes larger under open-circuit condition, the average force in the y-direction ( $F_y$ ) becomes smaller, as shown in Fig. 23(c). For static eccentricity, there is nearly no force in the y-direction.

The calculation time of NCRHM, CPM, and FEM for predicting the ESPM motor with static eccentricity is compared in Table II. The simulation setting is given in Table III

TABLE II  
CALCULATION TIME OF NCRHM UNDER STATIC ECCENTRICITY

Current (A)	0	4.2	7.7	11.6	15.5
NCRHM (s)	104	105	105	105	106
CPM (s)	162	163	163	163	164
FEA (s)	582	620	691	796	878

to guarantee a fair comparison. NCRHM can significantly accelerate the calculation for analyzing the rotor eccentricity fault in ESPM motors as it only costs less than one-fifth of the calculation time using FEM.



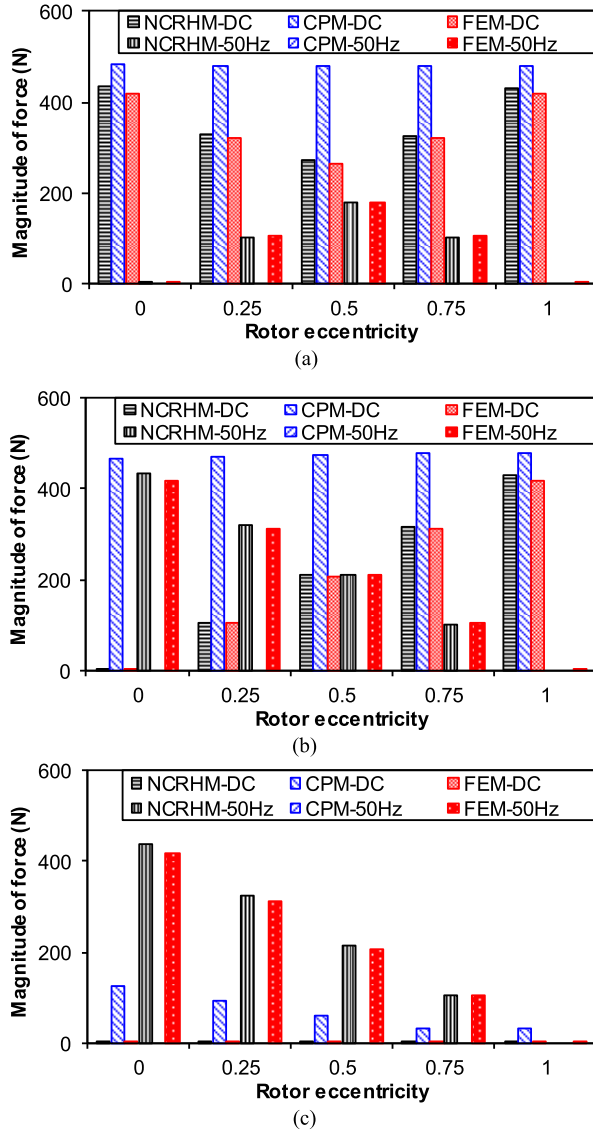


Fig. 23. Variation of major harmonic components of UMF with rotor eccentricity ratio for open-circuit condition: (a)  $F$ ; (b)  $F_x$ ; and (c)  $F_y$ .

TABLE III  
SIMULATION SETTING FOR NCRHM, CPM, AND FEM

Model	Airgap segment	Simulation steps	Total node	Total element
NCRHM	360	61	105	106
CPM	360	61	108	120
FEA	360	61	56481	108568

## V. CONCLUSION

This article proposed an NCRHM to accurately evaluate the impact of the rotor eccentricity, iron saturation, and slotting effect on the performance of ESPM motor. Four conformal mappings are applied to investigate rotor eccentricity and slotting effect on the air-gap field produced by the equivalent current. The saturation effect is represented using equivalent current of saturation, and it is extracted from the magnetic voltage drop on the stator iron. The proposed model can

accurately predict the total torque with asymmetric three-phase current, the cogging torque, and unbalance magnetic force under different rotor eccentricities. FEM results and experiment have verified the excellent accuracy and great efficiency of NCRHM. In the future, the proposed model can be improved to predict the performance of eccentric interior PM motor considering rotor saliency.

## REFERENCES

- [1] Z. Q. Zhu, L. J. Wu, and M. L. Mohd Jamil, "Influence of pole and slot number combinations on cogging torque in permanent-magnet machines with static and rotating eccentricities," *IEEE Trans. Ind. Appl.*, vol. 50, no. 5, pp. 3265–3277, Sep./Oct. 2014.
- [2] P. Jalali, S. T. Boroujeni, and N. Bianchi, "Analytical modeling of slotless eccentric surface-mounted PM machines using a conformal transformation," *IEEE Trans. Energy Convers.*, vol. 32, no. 2, pp. 658–666, Jun. 2017.
- [3] B. Ebrahimi, J. Faiz, and M. J. Roshkhari, "Static-, dynamic-, and mixed-eccentricity fault diagnoses in permanent-magnet synchronous motors," *IEEE Trans. Ind. Electron.*, vol. 56, no. 11, pp. 4727–4739, Nov. 2009.
- [4] P. Frauman, A. Burakov, and A. Arkio, "Effects of the slot harmonics on the unbalanced magnetic pull in an induction motor with an eccentric rotor," *IEEE Trans. Magn.*, vol. 43, no. 8, pp. 3441–3444, Aug. 2007.
- [5] E. Ajily, M. Ardebili, and K. Abbaszadeh, "Magnet defect and rotor eccentricity modeling in axial-flux permanent-magnet machines via 3-D field reconstruction method," *IEEE Trans. Energy Convers.*, vol. 31, no. 2, pp. 486–495, Jun. 2016.
- [6] J. Faiz, I. T. Ardekane, and H. A. Toliyat, "An evaluation of inductances of a squirrel-cage induction motor under mixed eccentric conditions," *IEEE Trans. Energy Convers.*, vol. 18, no. 2, pp. 252–258, Jun. 2003.
- [7] I. Tabatabaei, J. Faiz, H. Lesani, and M. Nabavi-Razavi, "Modeling and simulation of a salient-pole synchronous generator with dynamic eccentricity using modified winding function theory," *IEEE Trans. Magn.*, vol. 40, no. 3, pp. 1550–1555, May 2004.
- [8] A. Rahideh and T. Korakianitis, "Analytical open-circuit magnetic field distribution of slotless brushless permanent-magnet machines with rotor eccentricity," *IEEE Trans. Magn.*, vol. 47, no. 12, pp. 4791–4808, Dec. 2011.
- [9] L. S. Stephens and M. A. Casemore, "Influence of stator slot geometry and rotor eccentricity on field distribution in cylindrical magnetic actuators," *IEEE Trans. Magn.*, vol. 38, no. 2, pp. 1348–1356, Mar. 2002.
- [10] J. T. Li, Z. J. Liu, and L. H. A. Nay, "Effect of radial magnetic forces in permanent magnet motors with rotor eccentricity," *IEEE Trans. Magn.*, vol. 43, no. 6, pp. 2525–2527, Jun. 2007.
- [11] Y. Li, Q. Lu, Z. Q. Zhu, L. J. Wu, G. J. Li, and D. Wu, "Analytical synthesis of air-gap field distribution in permanent magnet machines with rotor eccentricity by superposition method," *IEEE Trans. Magn.*, vol. 51, no. 11, pp. 1–4, Nov. 2015.
- [12] D. G. Dorrell, "Experimental behaviour of unbalanced magnetic pull in 3-phase induction motors with eccentric rotors and the relationship with tooth saturation," *IEEE Trans. Energy Convers.*, vol. 14, no. 3, pp. 304–309, Sep. 1999.
- [13] F. Rezaee-Alam, B. Rezaeealam, and J. Faiz, "Unbalanced magnetic force analysis in eccentric surface permanent-magnet motors using an improved conformal mapping method," *IEEE Trans. Energy Convers.*, vol. 32, no. 1, pp. 146–154, Mar. 2017.
- [14] F. R. Alam and K. Abbaszadeh, "Magnetic field analysis in eccentric surface-mounted permanent-magnet motors using an improved conformal mapping method," *IEEE Trans. Energy Convers.*, vol. 31, no. 1, pp. 333–344, Mar. 2016.
- [15] H. Mahmoud and N. Bianchi, "Nonlinear analytical model of eccentric synchronous reluctance machines considering the iron saturation and slotting effect," *IEEE Trans. Ind. Appl.*, vol. 53, no. 3, pp. 2007–2015, May 2017.
- [16] T. A. Driscoll, *Schwarz-Christoffel Toolbox User's Guide: Version 2.3*, 2005.
- [17] Z. Q. Zhu, D. Howe, and C. C. Chan, "Improved analytical model for predicting the magnetic field distribution in brushless permanent-magnet machines," *IEEE Trans. Magn.*, vol. 38, no. 1, pp. 229–238, Jan. 2002.
- [18] L. J. Wu, Z. Q. Zhu, J. T. Chen, and Z. P. Xia, "An analytical model of unbalanced magnetic force in fractional-slot surface-mounted permanent magnet machines," *IEEE Trans. Magn.*, vol. 46, no. 7, pp. 2686–2700, Jul. 2010.

- [19] B. Hague, *Electromagnetic Problems in Electrical Engineering*. London, U.K.: Oxford Univ. Press, 1929.
- [20] J. Ren, X. Wang, and W. Zhao, "Magnetic field prediction of the saturated surface-mounted permanent magnet synchronous machine with rotor eccentricity," *IEEE Trans. Ind. Electron.*, vol. 69, no. 8, pp. 7756–7766, Aug. 2022.
- [21] L. Jing, Y. Pan, T. Wang, R. Qu, and P.-T. Cheng, "Transient analysis and verification of a magnetic gear integrated permanent magnet brushless machine with Halbach arrays," *IEEE J. Emerg. Sel. Topics Power Electron.*, vol. 10, no. 2, pp. 1881–1890, Apr. 2022.



**Zhuo Chen** (Graduate Student Member, IEEE) was born in Sichuan, China, in 1996. He received the B.S. degree in electrical engineering from Zhejiang University, Hangzhou, China, in 2018, where he is currently pursuing the Ph.D. degree in electrical machines and drives.

His current research interest is the design of permanent-magnet machines for aerospace and traction applications.



**Zhaokai Li** was born in Lishui, China, in 1993. He received the B.S. and Ph.D. degrees in electrical engineering from Zhejiang University, Hangzhou, China, in 2015 and 2020, respectively.

He is currently a Post-Doctoral Researcher with Zhejiang University. His major research interests include the analytical modeling of permanent magnet synchronous motor (PMSM) and iron loss analysis.



**Xiaoyan Huang** (Member, IEEE) received the B.E. degree in control measurement techniques and instrumentation from Zhejiang University, Hangzhou, China, in 2003, and the Ph.D. degree in electrical machines and drives from the University of Nottingham, Nottingham, U.K., in 2008.

From 2008 to 2009, she was a Research Fellow with the University of Nottingham. She is currently a Professor with the College of Electrical Engineering, Zhejiang University, where she is working on electrical machines and drives. Her research interests

are permanent-magnet (PM) machines and drives for aerospace and traction applications, and generator system for urban networks.



**Ang Liu** received the B.S. degree in electrical engineering from Zhejiang University, Hangzhou, China, in 2020, where he is currently pursuing the Ph.D. degree in electrical machines and drives.

His current research interest is the design and optimization of permanent-magnet machines for robotics and drones.



**Yelong Yu** was born in Zhejiang, China, in 1995. He received the B.Eng. degree in electrical engineering from Zhejiang University, Hangzhou, China, in 2018, where he is currently pursuing the Ph.D. degree in electrical engineering.

His research interests include the motor drive and control, and demagnetization fault diagnosis for permanent magnet synchronous motors (PMSMs).



**Lijian Wu** (Senior Member, IEEE) received the B.Eng. and M.Sc. degrees from the Hefei University of Technology, Hefei, China, in 2001 and 2004, respectively, and the Ph.D. degree from The University of Sheffield, Sheffield, U.K., in 2011, all in electrical engineering.

From 2004 to 2007, he was an Engineer with Delta Electronics (Shanghai) Company Ltd., Shanghai, China. From 2012 to 2013, he was a Design Engineer with the Sheffield Siemens Wind Power Research Center, Sheffield, focusing on wind power generators. From 2013 to 2016, he was an Advanced Engineer with Siemens Wind Power A/S, Brande, Denmark. Since 2016, he has been with Zhejiang University, Hangzhou, China, where he is currently a Professor of Electrical Machines and Control Systems. His major current research interest includes the design and control of permanent magnet machines.